IUST
Iran University of Science and Technology

Iranian Journal of Electrical and Electronic Engineering

Journal Homepage: ijeee.iust.ac.ir

Design and Analysis of a Minkowski Fractal Slot-Integrated UWB Antipodal Vivaldi Antenna for Brain Stroke Detection

Sowmya M*, Sumi M*(C.A.) and Harikrishnan A I*

Abstract: This article presents the design and optimization of a Minkowski fractal slot-integrated antipodal Vivaldi antenna (MFS-AVA) for brain stroke detection. The antenna is proposed on a 65 × 65 × 1.6 mm³ FR-4 substrate and integrates a tapered slot radiator with a microstrip feed. Key parameters are optimized through parametric analysis. The exponential curve of the radiator arms and edge conductor is fine-tuned for improved bandwidth and impedance matching, while Minkowski fractal slots enhance the reflection coefficient, gain, and directivity. Simulated using CST Studio Suite 2016, the antenna attains an extensive bandwidth spanning from 1.23 GHz to 12 GHz, a maximum gain of 9 dBi, and a radiation efficiency of 87%. The radiation pattern exhibits a directional beam with minimal side lobes, making it suitable for focused microwave imaging. Compared to a conventional design, the MFS-AVA shows improved S11, VSWR, and surface current performance. Its effectiveness is validated using a four-layered tissue-mimicking cylindrical human head model, confirming adequate field penetration and compliance with safety standards. These results demonstrate the proposed antenna's suitability for UWB microwave imaging in brain stroke detection.

Keywords: antipodal Vivaldi antenna, brain stroke detection, Minkowski fractal slot, tissue-mimicking head model, UWB microwave imaging.

1 Introduction

BRAIN stroke remains a critical public health challenge in 2025, with its global burden continuing to rise. Recent reports estimate that stroke incidence is increasing rapidly, with projections indicating 21.43 million new cases annually by 2050 which represents an 81% rise from 2021 levels [1]. The number of stroke-related deaths is also projected to increase from 6.6 million in 2020 to 9.7 million annually, with low- and middle-income countries (LMICs) bearing the highest mortality rates. Asia, which accounted for 61% of global stroke deaths in 2020, is projected to witness a rise to 69%, while Sub-Saharan Africa's stroke mortality could grow from 6% to 8%. Additionally, the economic cost of stroke is anticipated to escalate from $891 billion in 2017 to $2.31 trillion by 2050, making it one of the most financially burdensome diseases worldwide. Despite advancements in neuroimaging, AI-driven diagnostics, and minimally invasive treatments, several challenges persist in stroke management. The growing prevalence of hypertension, diabetes, obesity, and inactive lifestyles, particularly among younger populations, further exacerbates the issue. Moreover, disparities in access to acute stroke care, emergency response systems, and post-stroke rehabilitation continue to hinder effective treatment outcomes, especially in under-resourced regions [2]. Addressing these concerns through early detection, improved healthcare infrastructure, and large-scale public health interventions is crucial in mitigating

Iranian Journal of Electrical & Electronic Engineering, 2026.
Paper first received 09 May 2025 and accepted 18 Oct 2025.
* The author is with the Department of Electronics and Communication Engineering, NSS College of Engineering, Palakkad, Kerala, India.
E-mails: sowmyamohanan01@gmail.com, sumi@nssce.ac.in and harikrishnan.ai@nssce.ac.in.
Corresponding Author: Sumi M.

the long-term impact of stroke and reducing its mortality and disability burden [3].

Brain imaging approaches are essential for rapid analysis as well as management of brain diseases, with each modality offering specific advantages. Computed Tomography (CT) is the most widely used initial screening tool due to its speed and availability, making it ideal for detecting hemorrhagic strokes. CT Angiography (CTA) and CT Perfusion (CTP) further aid in assessing blood vessel blockages and cerebral blood flow, crucial for determining treatment strategies. While Magnetic Resonance Imaging (MRI) delivers superior contrast for soft tissues and is highly effective in detecting ischemic strokes, its higher cost and longer scan time limit its use in emergency settings. Diffusion-Weighted Imaging (DWI), a specialized MRI technique, is particularly useful in identifying acute ischemic strokes by detecting early changes in water diffusion. Transcranial Doppler Ultrasound (TCD) offers a portable and non-invasive option for monitoring cerebral blood flow, especially in high-risk patients. Although Positron Emission Tomography (PET) is less commonly used in acute stroke diagnosis, it provides metabolic insights valuable for assessing brain tissue viability. Advanced imaging techniques like Functional MRI (fMRI) and Perfusion-Weighted Imaging (PWI) help evaluate stroke recovery, while Electroencephalography (EEG) and Magnetoencephalography (MEG) are useful in detecting post-stroke complications such as seizures. The choice of imaging depends on stroke type, time since onset, and resource availability, with rapid diagnosis being critical for improving patient outcomes [4, 5].

Microwave Imaging (MI) with Ultra-Wideband (UWB) antennas is emerging as a promising tool for brain stroke detection, offering a non-ionizing, cost-effective, and portable alternative to MRI and CT [6]. By leveraging the dielectric contrast between healthy and stroke-affected tissues, MI enables early detection of ischemic and hemorrhagic strokes without the need for contrast agents or radiation exposure. Its compact and portable design allows for bedside and pre-hospital stroke assessment, making it particularly valuable for emergency settings and continuous monitoring.

Ultra-Wideband (UWB) antennas perform vital part in Microwave Imaging (MI) for brain stroke detection, offering high-resolution imaging over wideband frequency span, usually from 3.1 to 10.6 GHz. Their ability into penetrate biological tissues and distinguish different tissue types based on electromagnetic properties makes them highly effective for identifying stroke-affected regions. In stroke imaging, UWB systems capture reflected signals from multiple angles, enabling the reconstruction of detailed 3D images for precise localization of ischemic or hemorrhagic areas. Unlike static imaging methods such as MRI or CT, UWB-based systems provide real-time feedback, making them suitable for continuous monitoring and intraoperative guidance during stroke interventions [7].

Developing an efficient antenna for brain stroke detection requires an equilibrium between dimensions, bandwidth, and efficiency to ensure accurate imaging. Various designs have been proposed, each with its advantages and limitations. A wearable microstrip patch antenna measuring 33 × 23 × 1 mm³, operating between 2.4 GHz and 2.5 GHz, offers a safe Specific Absorption Rate (SAR), but its signal range is limited to 0.1 GHz, restricting imaging resolution [8]. A textile-based broadband antenna, aimed at stroke detection, operates from 1.13 GHz to 4.88 GHz, offering broad bandwidth. However, its omnidirectional radiation pattern leads to signal loss [9]. Another approach involves a low profile UWB antenna with a modified radiating patch and T-shaped slots on the ground plane. However, it struggles to penetrate deeper tissue layers due to its omnidirectional radiation pattern [10]. A Patch antenna with an inset feed, operating within 2.39 GHz to 2.46 GHz, offers excellent return loss (~ −60 dB), high gain, and a unidirectional radiation pattern, but its small bandwidth limits imaging accuracy, and it lacks testing on a head phantom to evaluate penetration depth [11]. A stacked patch 3D antenna, measuring 25 × 25 × 10.5 mm³, is designed for compactness and unidirectional radiation, achieving good directivity and acceptable gain, but its narrow bandwidth (2.65 GHz to 2.91 GHz) reduces imaging resolution [12]. Addressing these challenges requires further optimization in size, bandwidth, and penetration capability to enhance stroke detection accuracy.

The Vivaldi antenna, particularly its enhanced version, the Antipodal Vivaldi Antenna (AVA), has gained popularity in brain stroke imaging due to its ultrawideband (UWB) capabilities and efficient radiation characteristics. Research has explored UWB Vivaldi antennas, demonstrating their ability to operate over a broad frequency range, with some designs covering 0.4 GHz to 2.7 GHz. However, many of these studies focus primarily on return loss and Specific Absorption Rate (SAR) without fully evaluating the antenna's penetration depth and sensitivity when tested on a multi-layered head model. Another wideband tapered slot Vivaldi antenna, designed to function between 1 GHz and 4 GHz, shows promising performance, but its large physical size (95 × 90 × 1.28 mm³) pose a limitation for practical applications. Similarly, some AVA designs achieve wide bandwidth but remain bulky (329.25 × 153

× 1.6 mm³), making integration into portable imaging systems challenging. While these antennas offer wideband operation, their effectiveness in real-world stroke detection depends on improvements in size, penetration depth, and imaging accuracy, emphasizing the need for further optimization and experimental validation.

Further, to enhance the performance, researchers have explored various slot incorporation techniques. Among them, square and circular slots have been commonly investigated due to their simple geometry and ease of fabrication. For instance, [13] analyzed the use of rectangular slots in a Vivaldi antenna, achieving moderate bandwidth, while [14] utilized semi-circular slots to support wideband performance with smoother radiation patterns. However, while these basic geometries offer improvements, they often fall short in terms of multiband behaviour, miniaturization, and surface current control.

To address these limitations, researchers have explored the integration of fractal slot structures into antenna designs, significantly improving bandwidth, efficiency, and directivity. Among various fractal geometries, the Minkowski fractal has been widely studied for its ability to optimize impedance matching and radiation characteristics. Numerical analyses suggest that the second iteration of the Minkowski fractal provides the best balance between performance and design complexity. Various Minkowski-based configurations, including the Minkowski island, Minkowski curve, and Nested Minkowski, have demonstrated effectiveness in single-band and multiband operations, showcasing their adaptability. While researchers have extensively applied fractal geometries in antenna engineering, their incorporation into Antipodal Vivaldi Antennas (AVA) remains a relatively new development. The integration of a Minkowski fractal patch into AVA further enhances its broad bandwidth, strong directivity, and imaging resolution, making it a promising candidate for microwave visualizing and detection applications [15].

The paper introduces a Minkowski fractal slot-integrated ultra-wideband (UWB) antipodal Vivaldi antenna (MFS-AVA) engineered for microwave imaging (MWI) technologies. The antenna has a concise structure having a size of 65 × 65 × 1.6 mm³, a functional bandwidth ranging from 1.23 to 12 GHz, with a maximum gain of 9 dBi at 8 GHz. Then, the integration of the Minkowski fractal slot significantly enhances bandwidth, efficiency, and gain, ensuring improved signal penetration. These characteristics make it a promising solution for medical diagnostics, particularly in brain stroke detection and monitoring.

The manuscript is structured in the following manner: Section 2 describes antenna configuration and its specifications. Section 3 covers simulation and analysis, including parametric studies, frequency-domain performance, and evaluation with a four-layered tissue-mimicking cylindrical head phantom, focusing on E-field, H-field, and scattering parameters. Section 4 concludes with a summary of the main findings.

2 Antenna Configuration and Parameters

The structure and its parameters of proposed antipodal Vivaldi antenna (AVA) are shown in figure 1. This antenna is proposed on a dual-sided FR-4 substrate, which has dielectric constant of 4.4, with a loss factor of 0.019 and a height of 1.6 mm. Here, FR-4 is selected for its affordability and widespread availability. The AVA comprises two primary components: the converging radiator and the feed connection, as depicted in figure 1(a). The converging radiator consists of even conductive lobes, symmetrically positioned in either side of the substrate along the x-axis. The inner edges of these conductive arms are critical for studying the antenna's radiating features. The configuration in the proposed Minkowski fractal slot-loaded antipodal Vivaldi antenna (MFS-AVA) is depicted in figure 1(b). A microstrip feed is designed for the proposed antenna to align the input impedance with the antenna (50 Ω), ensuring proper signal transmission.

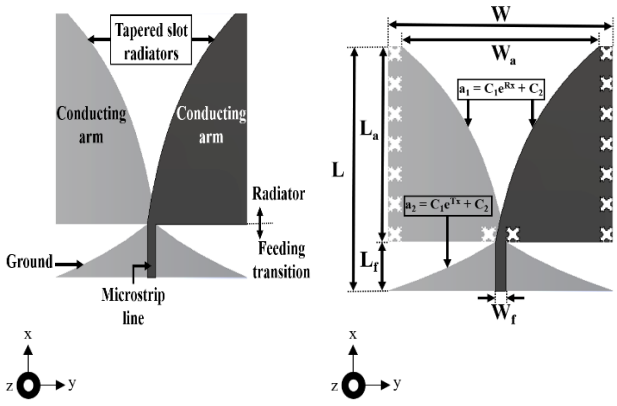

(a) (b)

Fig 1. Configuration of the proposed antenna and its variables (a) AVA (b) MFS-AVA.

Table 1. Proposed antenna variables.

Variable	Value(mm)	Variable	Value (mm)
L	65	W	65
L_a	52	W_a	57
L_f	13	W_f	3
R	0.036	T	-0.05

The proposed antenna has total dimensions of 65 × 65 × 1.6 mm³. The configuration is modeled using CST Studio Suite 2016, with its variables and values outlined in Table 1.

The entire size of the antipodal Vivaldi antenna (AVA) can be determined using Equations (1) and (2) as referenced in prior studies [16]. For efficient radiation, the antenna length (L) has to surpass half of the maximum effective wavelength (λ), while the width (W) should exceed one-quarter of it. This study focuses in the ultra-wideband (UWB) frequency domain of 3.1 GHz to 10.6 GHz, with the lowest frequency set at 3 GHz, corresponding to a wavelength of 100 mm. Thus, the antenna length should be at least 50 mm (λ/2) and the width at least 25 mm (λ/4). The Vivaldi antenna, well-suited for high-frequency applications, exhibits a strong end-fire radiation pattern above 3 GHz, ensuring efficient signal transmission across the UWB spectrum, as derived from substituting the wavelength values into the mentioned equations (1) and (2).

$$L > \frac{\lambda}{2} \tag{1}$$

$$W > \frac{\lambda}{4} \tag{2}$$

The curve of the radiating elements, denoted as a_1, and the edge ground, represented as a_2, in the antipodal Vivaldi antenna is designed using exponential formulas. These curves are specifically defined by Equations (3) and (4), as referenced in previous studies [17].

$$a_1 = C_1 e^{Rx} + C_2 \tag{3}$$

$$a_2 = C_1 e^{Tx} + C_2 \tag{4}$$

In this arrangement, the curvature constant R is set at 0.036, with T assigned a value of -0.05, while x represents the x-axis points along the curvature route. The curvature constant of the radiating elements is adjusted based for the intended antenna performance, taking into consider variables like frequency range, and emission profile. Through optimization, a curvature rate of 0.036 is found to yield the lowest reflection coefficient, keeping values under -10 dB in this study. Meanwhile, C_1 and C_2 are defined according to Equations (5) and (6) as indicated in a previous research [18].

$$C_1 = \frac{y_2 - y_1}{e^{Rx_2} - e^{Rx_1}} \tag{5}$$

$$C_2 = \frac{y_1 e^{Rx_2} - y_2 e^{Rx_1}}{e^{Rx_2} - e^{Rx_1}} \tag{6}$$

The coordinates (x_1, y_1) and (x_2, y_2) in Equations (5) and (6) represent initial as well as final points concerning the curved paths corresponding to the radiating elements and the edge ground, respectively.

To further analyze performance, parametric variations were introduced in tapered slit dimension (L_a), transmission line dimension (L_f), and transmission line width (W_f), as these parameters significantly impact current flow and radiation characteristics.

The primary goals of incorporating the proposed Minkowski fractal slots are to improve the antenna's reflection coefficient, expand its bandwidth, and enhance its directivity. The mathematical methodology for designing a Minkowski fractal, as outlined in [19], was utilized in this study. The Minkowski fractal was created using Iterated Function System (IFS). Figure 2 illustrates

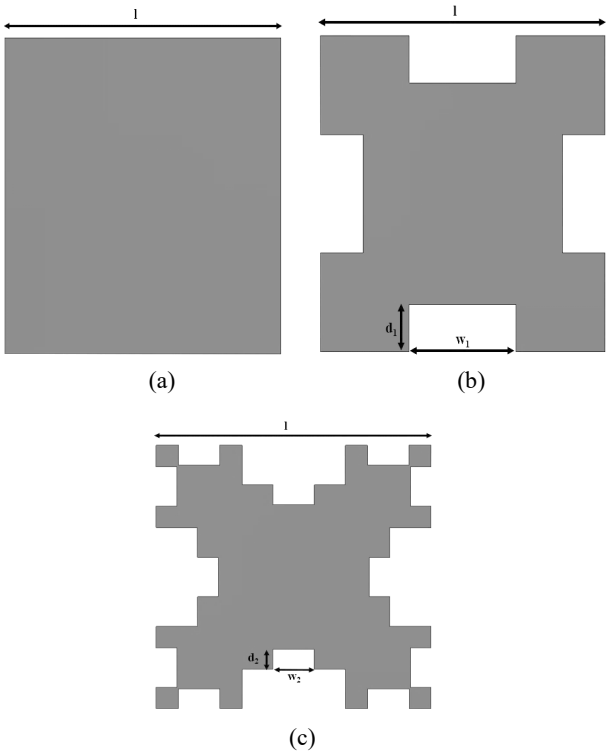

Fig 2. Iterations of Minkowski fractal slot (a) Initiator square patch (b) First order fractal (c) Second order fractal.

Table 2. Proposed Minkowski slot variables.

Variable	Value(mm)	Variable	Value (mm)
l	4	d_1	0.6
w_1	1.5	d_2	0.3
w_2	0.6	-	-

the iterative evolution of the Minkowski fractal with its variables and values outlined in Table 2. Beginning with an initiator square of the side length l. In the first iteration, rectangular slots of dimensions d_1 (length) and w_1 (width) are removed from each side of the square. Subsequently, in the second iteration, additional slots of size d_2 and w_2 are excised from all sides of the modified structure obtained after the first iteration.

3 Outcomes and Interpretation

3.1 Antenna performance simulation and assessment

This research intends to develop a superior antenna that works efficiently for neurological detection and imaging. To achieve this, various design parameters will be analyzed and refined. The return loss (S_{11}) will serve as primary metric to evaluate various variable values. Then, the impact of modifying the parameter L_a (with values 50 mm, 52 mm, and 54 mm) on the simulation results is illustrated in Figure 3(a). For L_a = 50 mm and L_a = 54 mm, the reflection coefficient rises above -10 dB, resulting in multiple bands instead of a single UWB response. A reflection coefficient above -10 dB indicates poor impedance matching and increased signal reflection. In contrast, L_a = 52 mm provides optimal performance, ensuring a well-matched impedance and a stable Ultrawideband (UWB) response. Secondly, the feedline length L_f is analyzed by varying it from 11 mm to 15 mm as illustrated in Figure 3(b). For L_f = 11 mm, the reflection coefficient remains mostly above -10 dB, indicating very poor performance. On the other hand, for L_f = 15 mm, the reflection coefficient rises above -10 dB around 7 GHz, that leads to the formation of two separate bands instead of a single UWB response. Overall, L_f = 13 mm provides good performance, ensuring proper impedance matching and stable UWB response. Finally, feedline width W_f is varied from 2.5 mm to 3 mm. For all values with this range, a UWB band is achieved with the reflection coefficient

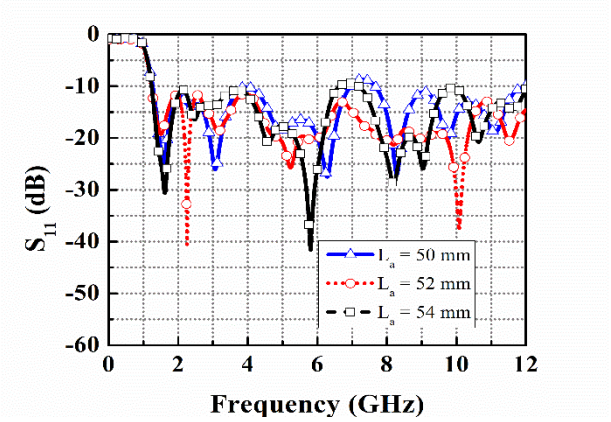

(a)

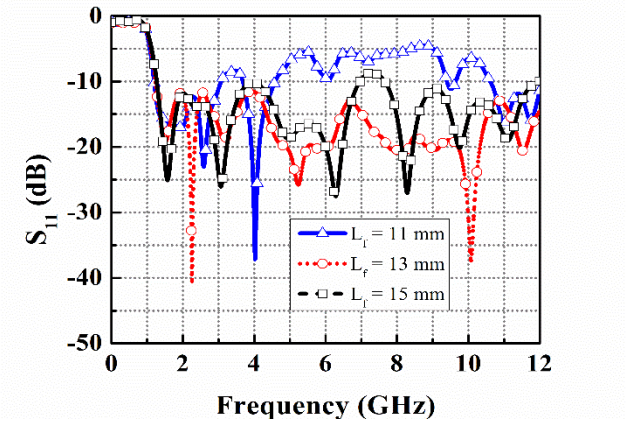

(b)

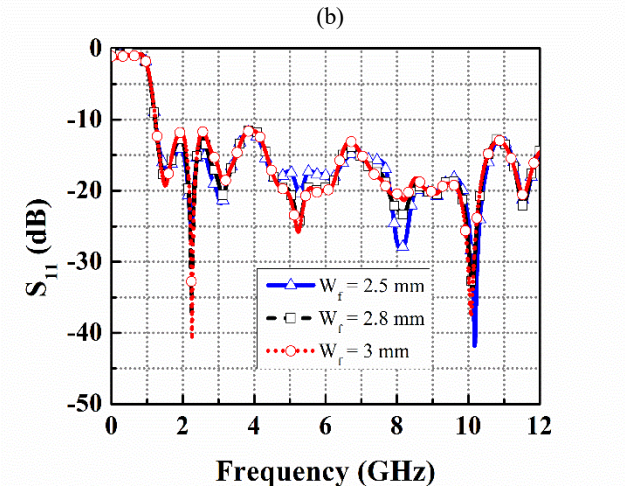

(c)

Fig 3. Reflection loss variation due to (a) L_a (b) L_f, and (c) W_f, for different lengths.

remaining below -10 dB, indicating good performance as shown in Figure 3(c). Since FR-4 is used as the substrate, W_f = 3 mm is the most suitable choice as it helps achieve a characteristic impedance of approximately 50 ohms. Therefore, W_f = 3 mm is considered for the final design.

The simulated reflection coefficient (S_{11}) of the traditional AVA (T-AVA) and the Minkowski fractal slot-integrated AVA (MFS-AVA) is compared in Figure 4(a). The T-AVA exhibits multiple resonance bands, with the first spanning 1.23 GHz to 1.9 GHz, the second from 2.19 GHz to 3.71 GHz, and the third covering 4.82 GHz to the UWB range. However, the MFS-AVA achieves a continuous wideband response, operating from 1.23 GHz to 12 GHz, ensuring seamless coverage across the entire UWB spectrum. This enhancement is attributed to the Minkowski fractal slot incorporation, which improves the impedance matching, enhances bandwidth, and reduces reflections. The voltage standing wave ratio (VSWR) remains below the threshold of 2 throughout the operating band, indicates efficient power

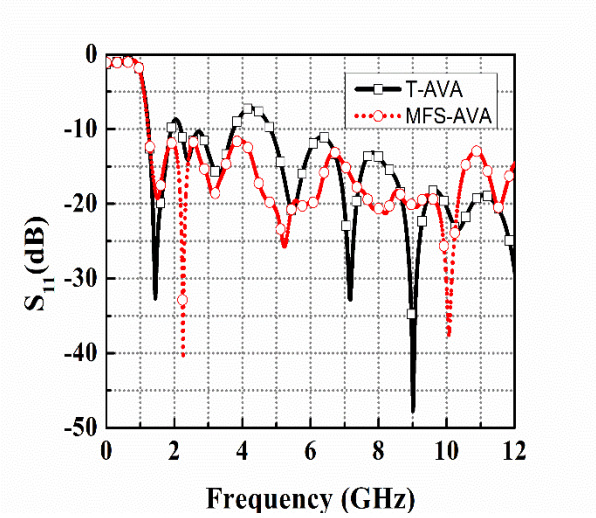

(a)

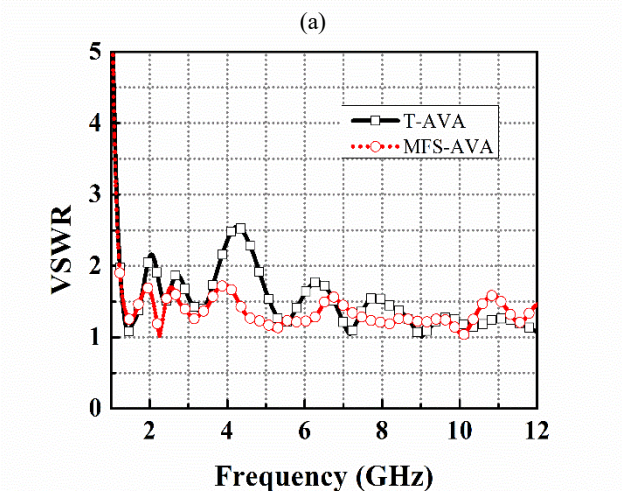

(b)

Fig 4. Simulated (a) reflection loss and (b) VSWR plot of the proposed antenna.

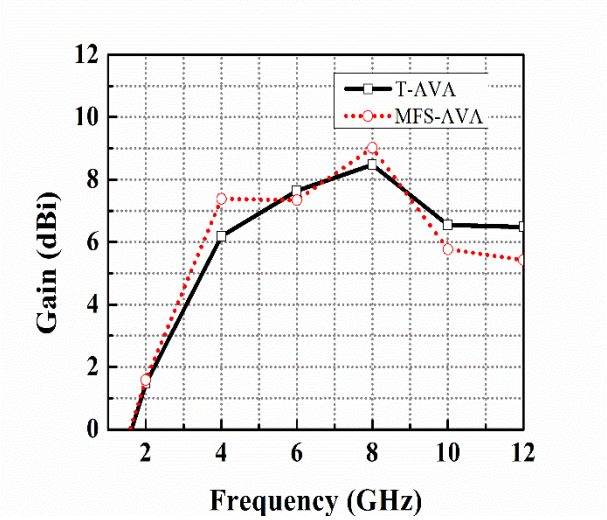

(a)

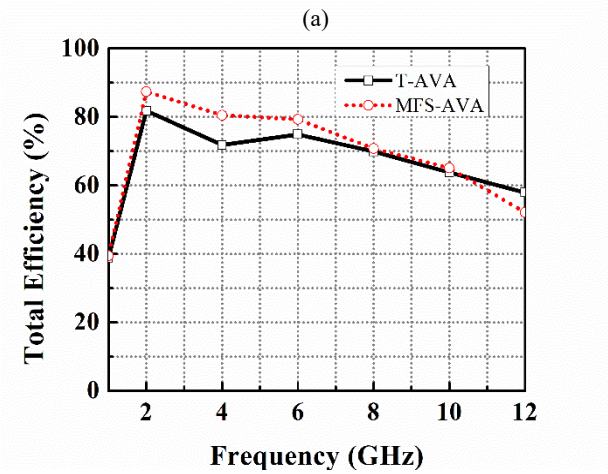

(b)

Fig 5. Simulated (a) realized gain and (b) total efficiency plot of the proposed antenna.

transfer and good impedance matching as depicted in Figure 4(b). The increased frequency span and the better performance make the MFS-AVA more effective than the conventional counterpart, the T-AVA. Next, Figure 5 (a) illustrates the antenna gain across its operating frequency range. The MFS-AVA demonstrates good performance, achieving a peak gain of 9 dBi at 8 GHz, whereas the T-AVA achieves a peak gain of 8.6 dBi at same frequency. This represents a 0.4 dBi increase in gain for the MFS-AVA, indicating its improved radiation performance compared to the T-AVA. Figure 5(b) depicts the total radiation efficiency of both the traditional and proposed antennas. It is observed that the T-AVA exhibits a radiation efficiency of 81%, whereas the MFS-AVA achieves a higher radiation efficiency of 87%. This represents a 6% improvement in total radiation efficiency for the MFS-AVA, considering all losses. The enhanced efficiency of the MFS-AVA indicating better overall performance, with lesser energy loss, leading to improved signal transmission and greater reliability in practical applications.

Figure 6(a) shows the distribution of surface current at 2.25 GHz, where the currents are primarily concentrated in the feed area, then along tapered slot radiator, and in the minkowski slots located along the edges of the radiator. This distribution leads to resonance at 2.25 GHz. in Figure 6(b), the distribution of surface current at 5.2 GHz is shown, with currents concentrated on the upper and bottom curvatures of the tapered slot radiator, as well as in the feeding section. This concentration is main reason for resonance at 5.2 GHz. Ultimately, Figure 6(c) shows distribution of surface current at 10 GHz, wherein the current is predominantly concentrated along the tapered slot radiator and the feed line, resulting

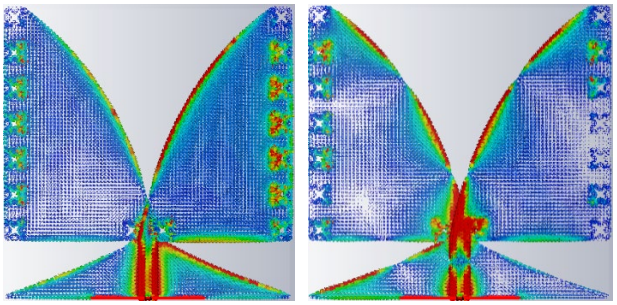

(a) (b)

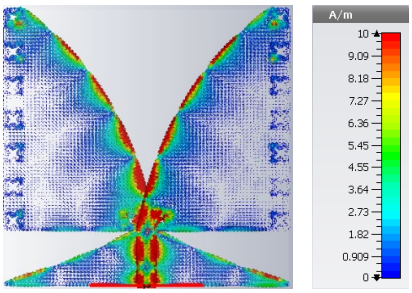

(c)

Fig 6. Distribution of surface current at (a) 2.25 GHz, (b) 5.2 GHz, and (c) 10 GHz.

resonance at 10 GHz. These variations in distribution of surface current at various frequencies highlight the antenna's resonant behavior and its ability to efficiently operate at multiple frequencies.

The antenna's beam pattern characteristics will be comprehensively discussed next. Figure 7 depicts the beam patterns of both traditional T-AVA and the Minkowski slot-integrated antipodal Vivaldi antenna (MFS-AVA) exhibiting a highly directional pattern with minimal side lobes. The major lobes are focused in beam aligned X-direction, ensuring efficient radiation along the intended path. The patterns demonstrate good stability across different frequencies. This unidirectional behavior is crucial for applications requiring focused radiation and minimal back-lobe radiation. The introduction of Minkowski slots in the proposed design further enhances radiation performance by improving impedance matching and reducing unwanted side lobes.

3.2 Antenna analysis using human head model

In this section, the effectiveness of the proposed antenna for use with a human head model are assessed. This evaluation is crucial to determine its effectiveness in head imaging, particularly in terms of signal penetration depth, response variations between healthy and unhealthy brain tissues, also specific absorption rate (SAR). The human head consists of multiple tissue layers, including skin, fat, skull, cerebrospinal fluid (CSF), and brain, that is further divided into grey and white substance. Each of these tissues exhibits distinct permittivity and conductivity properties [20], making microwave imaging a viable approach due to its dependence on dielectric contrast for image reconstruction. Table 3 provides details on the dielectric behavior of various head tissues.

A four-layered cylindrical tissue-mimicking head model is considered for analysis. Figure 8 presents the schematic representation of four layers of the cylindrical tissue-mimicking head phantom. The radius of the outer skin layer measures 40 mm, followed by skull at 36 mm,

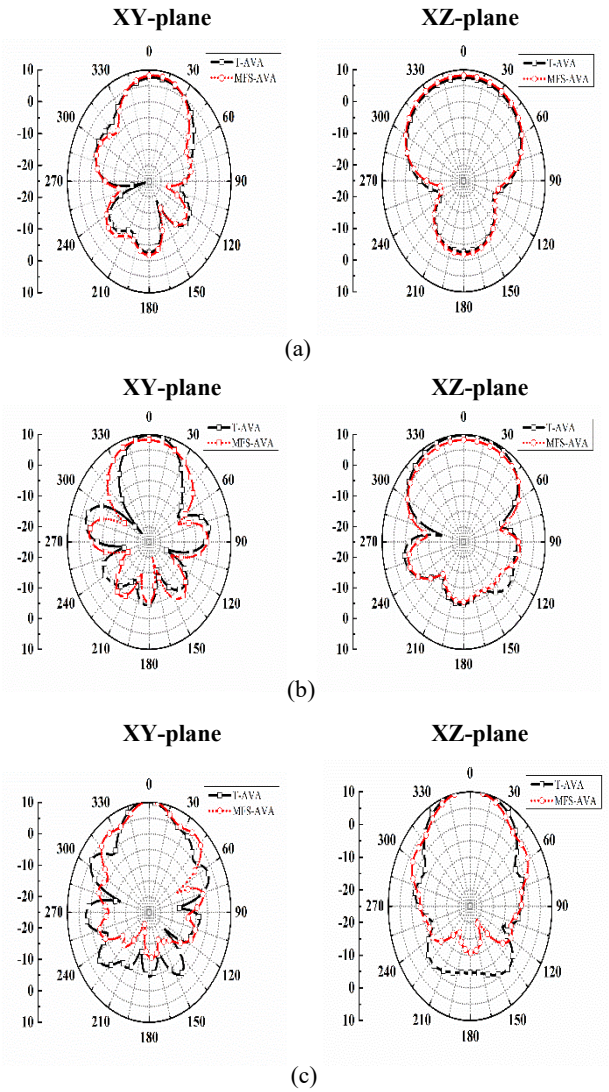

Fig 7. Radiation pattern of T-AVA and MFS-AVA in both xy-plane and xz-plane at (a) 4 GHz, (b) 6 GHz, and (c) 8 GHz.

Table 3. Dielectric behavior of head tissues.

Type of tissue	Relative dielectric constant, ε_r	Conductivity, σ (S/m)
Skin	43	0.89
Fat	5.44	0.05
Skull	12.36	0.15
CSF	68.43	2.45
Grey substance	52.28	0.98
White substance	38.57	0.62

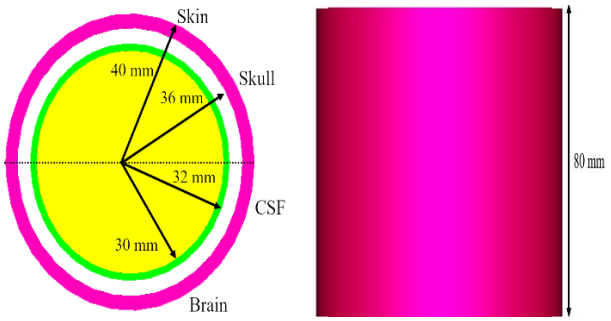

(a) (b)

Fig 8. Schematic depiction of the four-layered head model, (b) Cylindrical head phantom model.

the cerebrospinal fluid (CSF) at 32 mm, and finally, the brain at 30 mm. The cylindrical model is designed with a height of 80 mm to closely resemble the anatomical structure for accurate evaluation. Figure 9 represents the schematic representation of the four layered tissue mimicking head phantom, along with different views of the phantom with the Minkowski slot-integrated antenna positioned 20 mm away from the skin layer. This configuration ensures optimal interaction between the antenna and the head phantom, facilitating accurate evaluation of antenna's performance for brain scanning purposes.

The E-field as well as H-field penetration through head model is pivotal for assessing antenna performance for brain imaging applications. When the electromagnetic signal propagates via tissue strata, intensity of both fields gradually decreases because of the inherent loss in biological tissues. The E-field is responsible for inducing currents within the tissues, while H-field will govern the

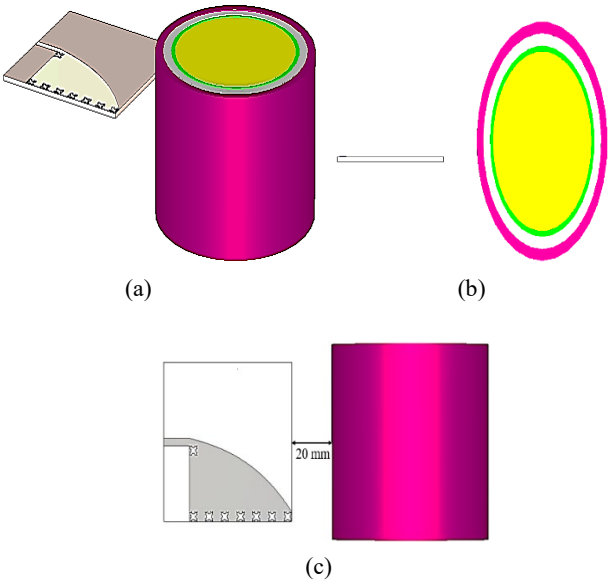

(a) (b)

(c)

Fig 9. Antenna placement near head model (a) Outlook view, (b) Top view, and (c) Front view

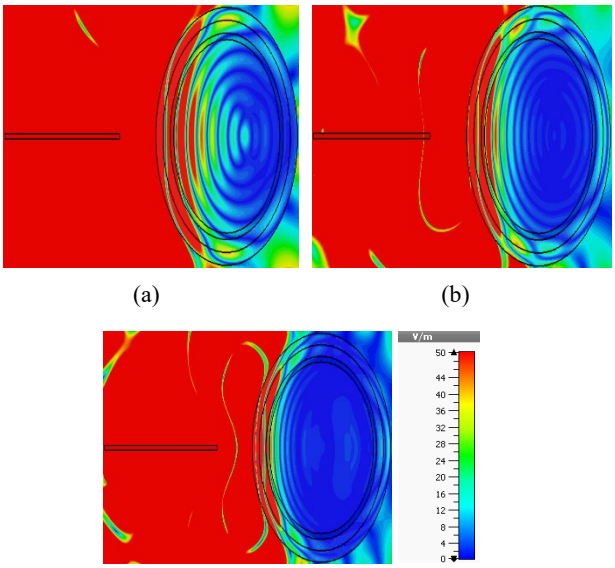

(a) (b)

(c)

Fig 10. E-field distribution demonstrating the extent of penetration within the head model at (a) 4 GHz, (b) 6 GHz, and (c) 8 GHz.

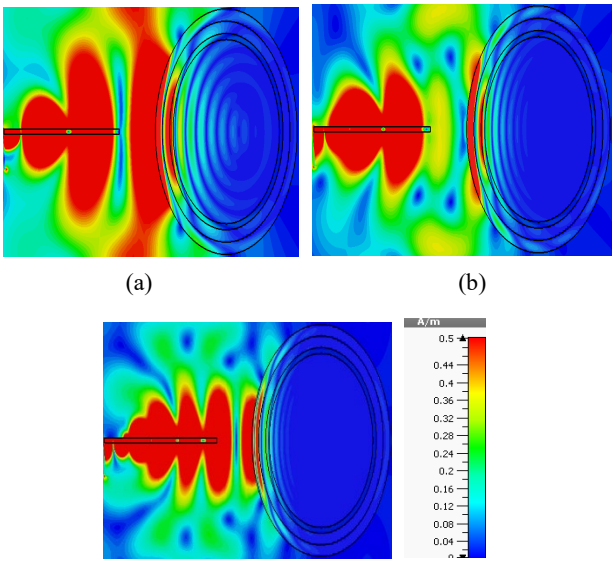

(a) (b)

(c)

Fig 11. H-field distribution demonstrating the extent of penetration within the head model at (a) 4 GHz, (b) 6 GHz, and 8 GHz.

the magnetic response of the medium. The ability of these fields to effectively penetrate the head model determines the feasibility of detecting anomalies such as brain strokes. Figure 10(a–c) illustrates E-field distribution on the XZ-plane inside the four-layered head phantom at 4 GHz, 6 GHz, and 8 GHz, correspondingly. The findings show that electric field (E-field) effectively penetrates through different brain tissues, attaining a considerable penetration depth. Likewise, Figure 11(a–c) presents magnetic field (H-field) penetration inside head

phantom at corresponding frequencies, showcasing how H-field propagates, penetrates and also interaction with four different tissue layers present in the tissue mimicking head model. Although the H-field intensity diminishes as it propagates through head model, the antenna has directional radiation features enhances the penetration of electromagnetic (EM) fields. The analysis of electric field and magnetic field penetration confirms that proposed antenna efficiently interacts with head tissues, making it a suitable candidate for brain stroke imaging applications.

To simulate the occurrence of a stroke, a blood clot is strategically introduced within the tissue-mimicking cylindrical head model to replicate abnormal conditions in brain tissues. This setup helps to evaluate the antenna's ability to detect variations caused by stroke-like anomalies. Figure 12(a) present schematic representation of the stroke scenario, where the blood clot is embedded within the head model, and the Minkowski slot-integrated antenna is positioned 20 mm away from the outer dermal layer. Figure 12(b) illustrates a close-up of the blood clot, having radius (R) of 5 mm. The performance of proposed antenna is further evaluated based on its interaction with a simulated blood clot within the tissue-mimicking human model. The simulation results clearly indicate a distinct difference in the return loss between healthy as well as unhealthy head. In case of healthy head, a consistent ultra-wideband (UWB) response is observed across the frequency range of 1.23 to 10.6 GHz, remaining below the –10 dB threshold, that indicates low reflection. However, when a blood clot is present, the reflection coefficient curve deviates significantly, with portions rising above –10 dB. This leads to formation of separate bands instead of a continuous UWB response as illustrated in Figure 13. The alteration in antenna response is due to the high dielectric properties of the blood clot, which disrupt the propagation of electromagnetic waves through the different layers of head.

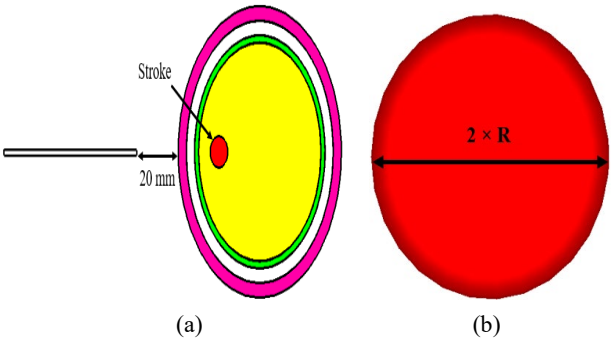

Fig 12. (a) Schematic representation of the head model with stroke condition, and (b) Stroke region with dimensions.

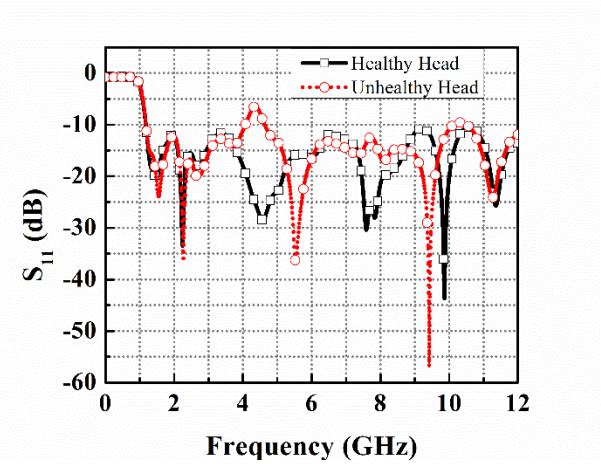

Fig 13. Simulated return loss of proposed antenna with healthy as well as unhealthy head.

The evaluation of the Specific Absorption Rate (SAR) is essential for imaging process, as it determines the permissible exposure limits of electromagnetic radiation to the human body, ensuring effectiveness during diagnosis. The evaluation of SAR can be carried out using the subsequent formula:

$$\mathrm{SAR} = \frac{|E|^2 \sigma}{M} \tag{7}$$

Here, |E| signifies the root mean square magnitude of the electric field, ρ represents the mass density, and σ refers to the electrical conductance of the head tissue. The Specific Absorption Rate (SAR) for the proposed antenna with the tissue-representative head model is calculated using CST Studio Suite 2016 for the frequencies 2 GHz, 4 GHz, 6 GHz, 8 GHz, and 10 GHz. A power input of 1 mW is utilized for the simulation. The SAR results from the simulation are presented in Table 4. The table indicates that the highest SAR value attained from the activation of the proposed antenna is 0.0115 W/kg for 1 g at 8 GHz and 0.00844 W/kg for 10 g at 1 GHz. In accordance with regulatory standards, the United States imposes a Specific Absorption Rate (SAR) ceiling of 1.6 W/kg averaged over 1 gram of tissue, while the European Union defines a limit of 2 W/kg averaged over 10 grams of tissue. SAR data obtained from simulation falls below limits, affirming the safe operation of antenna for head imaging applications.

Frequency (GHz)	SAR (1g) (W/kg)	SAR (10g) (W/kg)
2	0.00105	0.00844
4	0.0039	0.00242
6	0.00602	0.00425
8	0.0115	0.00573
10	0.00694	0.00363

Table 4. A comprehensive evaluation of the proposed antenna against related works.

Ref.	Antenna Structure	Dimensions (mm^3)	Substrate	Operating Band (GHz)	FBW (%)	Max. Gain (dBi)	Phantom Model	SAR (W/Kg)
[21]	Inverted delta shaped wideband antenna	50 × 44 × 1.524	Rogers RO4350B	1.70 – 3.71	74.3	5.65	Simulated Hugo head model	0.0023
[22]	Zero-Index metamaterial super substrates UWB antenna	110 × 65 × 0.51	Rogers Duroid RT5880	0.0 – 4.0	200	5.66	Liquid head phantom model	NG
[23]	Wearable microstrip antenna	33 × 23 × 1	FR-4	2.4 – 2.5	4.08	NG	Simulated head phantom model	0.48
[24]	Compact UWB bowtie antenna	60 × 60 × 50	Rogers RO4003C	1.0 – 6.0	143	NG	Liquid head phantom model	NG
[25]	Defected ground based UWB antenna	50 × 50 × 1.5	Rogers RO3003	2.94 – 6.96	81.2	3.93	Six-layered head model	NG
[26]	Sierpinski arrowhead curve slot antipodal Vivaldi antenna	65 × 65 × 1.6	Rogers RO4350B	2.35 – 3.79	46.9	7.35	Simulated Hugo head model	0.0013
[27]	U-shaped patch and W-shaped slot low SAR patch antenna	64 × 42 × 1.6	FR-4	1.40 – 2.52	57.14	3.5	Simulated Hugo head model	0.26
[28]	Dual cavity rectangular patch with etched ground antenna	70 × 60 × 1.6	FR-4	1.22 – 3.04	85.71	5.0	Simulated Hugo head model	0.608
[29]	UWB rectangular patch antenna	38 × 25 × 1.73	FR-4	5.26 – 8.5	47.09	3.33	Simulated head phantom model	0.3547
[30]	UWB graphene-based patch antenna	22 × 12 × 1.52	Rogers Laminate TMM4	3.15 – 9.15	97.5	NG	Simulated head phantom model	0.766
[31]	Waveguide-fed split-ring resonator antenna	24 × 24 × 1.6	FR-4	0.5 – 6.0	169	NG	Simulated head phantom model	0.007
[This Work]	**Minkowski fractal slot-integrated UWB antipodal Vivaldi antenna**	**65 × 65 × 1.6**	**FR-4**	**1.23 – 12.0**	**162.8**	**9.0**	**Four-layered tissue-mimicking cylindrical head model**	**0.00105**

NG = Not given; FBW = Fractional bandwidth.

The comparison of the antenna with related works and the proposed antenna is shown in Table 4, highlighting its superior performance for microwave head imaging. To summarize, it can be deduced that the proposed antenna achieves broad frequency performance, elevated gain, and a minimal SAR level. Additionally, throughout the analysis, the proposed antenna exhibits efficient penetration through the cranial tissue layers, facilitating interaction between the signal and the stroke.

4 Conclusion

This paper outlines the design and enhancement of a compact Minkowski slot-integrated antipodal Vivaldi antenna (MFS-AVA) specifically developed for brain stroke detection through ultra-wideband microwave imaging. The antenna accomplishes an expansive impedance bandwidth, high directivity, and efficient radiation with a focused emission pattern, making it well-suited for deep tissue penetration and superior imaging performance. The inclusion of Minkowski fractal slots contributes to notable improvements in return loss, VSWR, and surface current distribution when compared to conventional counterparts. The antenna's performance has been validated using a four-layered tissue-mimicking cylindrical head model, demonstrating both effective electromagnetic wave propagation and adherence to safety standards. Future research should focus on realistic head phantoms to better simulate human tissue properties and antenna arrays to enhance spatial resolution and improve image reconstruction in microwave imaging.

Conflict of Interest

The authors report no conflict of interest.

Funding

No funding was received for this work.

References

[1] V. L. Feigin, B. A. Stark, C. O. Johnson, G. A. Roth, C. Bisignano, and A. Abady, "Global, regional, and national burden of stroke and its risk factors, 1990–2019: A systematic analysis," *The Lancet Neurology*, vol. 21, no. 10, pp. 877–917, 2022.

[2] E. S. Donkor, "Stroke in the 21st century: A snapshot of the burden, epidemiology, and quality of life," *Stroke Research and Treatment*, vol. 2018, pp. 1–8, 2018, Article ID 3238165.

[3] R. V. Krishnamurthi, A. E. Moran, V. L. Feigin, S. Barker-Collo, B. Norrving, and G. A. Mensah, "Stroke prevalence, mortality, and disability-adjusted life years in 195 countries and territories, 1990–2030," *International Journal of Stroke*, vol. 15, no. 3, pp. 310–323, 2020.

[4] Ostrom, Q. T., M. Price, C. Neff, G. Cioffi, K. A. Waite, C. Kruchko, and J. S. Barnholtz-Sloan, "CBTRUS statistical report: Primary brain and other central nervous system tumors diagnosed in the United States in 2016-2020," *Neuro-Oncology*, Vol. 25, No. 4, iv1–iv99, Oct. 2023.

[5] Bhimani, A. D., S. Denyer, D. R. Esfahani, J. Zakrzewski, T. M. Aguilar, and A. I. Mehta, "Surgical complications in intradural extramedullary spinal cord tumors-an ACS-NSQIP analysis of spinal cord level and malignancy," *World Neurosurgery*, Vol. 117, e290–e299, 2018.

[6] M. T. Islam, M. T. Islam, M. Samsuzzaman, H. Arshad, and H. Rmili, ''Metamaterial loaded nine high gain Vivaldi antennas array for microwave breast imaging application,'' *IEEE Access*, vol. 8, pp. 227678–227689, 2020.

[7] Asok, A. O., G. N. S. J., and S. Dey, "Non-invasive breast tumor detection with antipodal vivaldi antenna using monostatic approach," *International Journal of RF and Microwave ComputerAided Engineering*, Vol. 32, No. 12, e23539, 2022.

[8] R. Raihan, M. S. A. Bhuiyan, R. R. Hasan, T. Chowdhury, and R. Farhin, ''A wearable microstrip patch antenna for detecting brain cancer,'' *in Proc. IEEE 2nd Int. Conf. Signal Image Process. (ICSIP)*, Aug. 2017, pp. 432–436.

[9] X. Lin, Y. Chen, B. Seet, F. Xia, Q. Zhang, and J. Hu, ''Compact textile wideband antenna for wearable microwave stroke imaging,'' *in Proc. 13th Eur. Conf. Antennas Propag. (EuCAP*), pp. 1–5, Mar. 2019.

[10] F. Ahmed, N. Hasan, and M. H. M. Chowdhury, "A compact low-profile ultra wideband antenna for biomedical applications," in *2017 Int. Conf. Electr., Comput. Commun. Eng. (ECCE)*, Dhaka, Bangladesh, pp. 87–90, Feb. 2017.

[11] A. Ahmed, M. N. Mollah, and A. Shihavuddin, "Tumor detection by rectangular microstrip patch antenna," in *Proc. 3rd Int. Conf. Sustain. Technol. Ind.*, pp. 1–5, Dec. 2021.

[12] N. G. Gunaseelan, V. A. Velvizhi, K. Jeyapiriya, and S. Gayathri, "Design of microwave 3-D antenna for brain tumour sensing system," in *Proc. Int. Conf. Commun., Comput. Internet Things*, pp. 1–4, Mar. 2022.

[13] K. S. Naik, D. Madhusudan, and S. Aruna, "Slot tapered Vivaldi antenna with corrugated edges," *Advanced Science and Technology Letters*, vol. 147, pp. 142–149, 2017.

[14] J. Seo, J. H. Kim, and J. Oh, “Semicircular patch-embedded Vivaldi antenna for miniaturized UWB radar sensors,” *Sensors*, vol. 20, no. 21, p. 5988, Oct. 2020.

[15] V. Jagadeesan, D. Venkatachalam, V. M. Vinod, A. K. Loganathan, S. Muthusamy, M. Krishnamoorthy, and M. Geetha, "Design and development of a new metamaterial sensor-based Minkowski fractal antenna for medical imaging," *Applied Physics A*, vol. 129, no. 5, pp. 391, 2023.

[16] A. S. Dixit and S. Kumar, "A survey of performance enhancement techniques of antipodal Vivaldi antenna," *IEEE Access*, vol. 8, pp. 45774–45796, 2020.

[17] A. M. De Oliveira, J. F. Justo, M. B. Perotoni, S. T. Kofuji, A. G. Neto, R. C. Bueno, and H. Baudrand, "A high directive Koch fractal Vivaldi antenna design for medical near-field microwave imaging applications," *Microw. Opt. Technol. Lett.*, vol. 59, no. 2, pp. 337–342, Feb. 2017.

[18] Z. Tahar, X. Dérobert, and M. Benslama, "An ultra-wideband modified Vivaldi antenna applied to through the ground and wall imaging," *Progress in Electromagnetics Research C*, vol. 86, pp. 111–122, 2018.

[19] N. P. Udeze, S. I. Orakwue, and M. I. Ehikhamenle, "Design of a tri-band Minkowski fractal MIMO antenna for FR2 5G applications," *Journal of Engineering Research and Reports*, vol. 26, no. 9, pp. 190–205, 2024.

[20] S. Wakim and M. Grewal, *Human Cells and Tissues* [Online]. Available: https://bio.libretexts.org/@go/page/16776, Dec. 13, 2021.

[21] A. Hossain, M. T. Islam, M. E. Chowdhury, and M. Samsuzzaman, "A grounded coplanar waveguide-based slotted inverted delta-shaped wideband antenna for microwave head imaging," *IEEE Access*, vol. 8, pp. 185698–185724, 2020.

[22] E. Razzicchia, I. Sotiriou, H. Cano-Garcia, E. Kallos, G. Palikaras, and P. Kosmas, "Feasibility study of enhancing microwave brain imaging using metamaterials," *Sensors,* vol. 19, no. 24, pp. 5472, 2019.

[23] M. A. Alzabidi, M. A. Aldhaeebi, and I. Elshafiey, "Optimization of UWB Vivaldi antenna for tumor detection," in *Proc. 2013 1st Int. Conf. on Artificial Intelligence, Modelling and Simulation*, pp. 81–86, Dec. 2013.

[24] O. Fiser, V. Hruby, J. Vrba, T. Drizdal, J. Tesarik, J. Vrba Jr., and D. Vrba, “UWB bowtie antenna for medical microwave imaging applications,” *IEEE Transactions on Antennas and Propagation*, vol. 70, no. 7, pp. 5357–5372, 2022.

[25] P. Z. Widyatama, B. S. Nugroho, and L. O. Nur, "Design of circular modified UWB antenna microstrip for brain cancer detection," in *Proc. 2019 IEEE Asia Pacific Conf. Wireless Mobile (APWiMob)*, pp. 33–36, Nov. 2019.

[26] M. Y. I. Yazid, M. H. Baharuddin, M. S. Islam, M. T. Islam, and A. F. Almutairi, "A Sierpinski arrowhead curve slot Vivaldi antenna for microwave head imaging system," *IEEE Access*, vol. 11, pp. 32335–32347, 2023.

[27] M. M. Alam, M. S. Talukder, M. Samsuzzaman, A. I. Khan, N. Kasim, I. M. Mehedi, and R. Azim, "W-shaped slot-loaded U-shaped low SAR patch antenna for microwave-based malignant tissue detection system," *Chinese J. Phys.*, vol. 77, pp. 233–249, 2022.

[28] M. Samsuzzaman, K. A. Fakeeh, M. S. Talukder, M. M. Hasan, M. H. Rahman, M. M. Alam, ... and M. T. Islam, "A double hollow rectangular-shaped patch and with the slotted ground plane monopole wideband antenna for microwave head imaging applications," *Int. J. Commun. Syst.*, vol. 34, no. 16, e4958, 2021.

[29] N. Goswami and M. A. Rahman, "Design of a UWB patch antenna and performance evaluation in detecting brain tumors," *e-Prime-Adv. Electr. Eng., Electron. Energy*, vol. 8, p. 100623, 2024.

[30] M. A. I. Aziz, M. M. Rana, M. A. Islam, and R. Inum, "Effective modeling of GBC based ultra-wideband patch antenna for brain tumor detection," in *2018 Int. Conf. Comput., Commun., Chem., Mater. Electron. Eng. (IC4ME2)*, pp. 1-4, 2018.

[31] P. Goodarzi, "A novel UWB antenna integrated with active circuit for high resolution near field microwave brain imaging," *Authorea Preprints*, 2023.

Sowmya M received the B. Tech. degree in Electronics and Communication Engineering from Government Engineering College, Palakkad, Kerala, India, in 2023, and the M. Tech. degree in Communication Engineering from NSS College of Engineering, Palakkad, Kerala, India, in 2025. Her research interests include Microwave Imaging, Ultra-Wideband (UWB) Antennas, and Compact Antennas.

Sumi M received the B. Tech degree in Electronics and Communication from the Cochin University of Science and Technology (CUSAT) in 2003, and the MTech degree in Electronic Design from the Indian Institute of Science in 2009 and received PhD from CUSAT in 2017. Her research interests are designing of Chipless RFID sensors, Microwave filters, Multiband and Ultra-wide band antennas.

Harikrishnan A I received B. Tech degree in Electronics and Communication Engineering from Mahatma Gandhi University, Kottayam, India and Master of Technology in Microelectronics and VLSI design from Indian Institute of Technology, Kharagpur, India. His research interests include planar antenna, reconfigurable microwave filters, Chipless RFID tags.